Hindawi
Geofluids
Volume 2021, Article ID 8348773, 20 pages
https://doi.org/10.1155/2021/8348773

Research Article

Pore Structure and Connectivity of Mixed Siliciclastic-Carbonate Tight Reservoirs in the Palaeogene from Qaidam Basin, NW China

Xin Wang,[1,2] Jianhui Zeng,[1,2] Kunyu Wu,[3] Xiangcheng Gao,[4] Yibo Qiu,[4] Tongzhi Lu,[1,2] Kunkun Jia,[1,2] Chen Zhang,[1,2] Juncheng Qiao,[1,2] Zixin Xue,[1,2] Qianyou Wang,[5] and Xiangye Kong[1,2]

[1]*College of Geosciences, China University of Petroleum, Beijing 102249, China*
[2]*State Key Laboratory of Petroleum Resources and Prospecting, China University of Petroleum, Beijing 102249, China*
[3]*Qinghai Oil Field Company, CNPC, Dunhuang, Gansu 736202, China*
[4]*Exploration and Development Institute, Shengli Oilfield Company, SINOPEC, Dongying, Shandong 257015, China*
[5]*Department of Earth, Ocean, and Ecological Sciences, University of Liverpool, Liverpool L69 3GP, UK*

Correspondence should be addressed to Jianhui Zeng; zengjh@cup.edu.cn

Received 8 July 2021; Revised 12 October 2021; Accepted 16 October 2021; Published 16 November 2021

Academic Editor: Afshin Davarpanah

The pore structure and connectivity in petroleum reservoirs are controlled in part by their petrological properties. Mixed siliciclastic-carbonate rocks have complex compositions and heterogeneous spatial distributions of the various minerals. As a result, the study of the pore structure and connectivity of mixed siliciclastic-carbonate tight reservoirs has been limited. In this study, methods such as thin section microscopy, X-ray diffraction, X-ray computed tomography, low pressure N_2 adsorption, and spontaneous imbibition were adopted to comprehensively analyze the petrological properties, pore structure, and connectivity of the mixed siliciclastic-carbonate tight reservoirs in the upper member of the Xiaganchaigou Formation in the Yingxi Area, Qaidam Basin. The results showed that micrometer-sized pores in mixed siliciclastic-carbonate tight reservoirs are mainly dissolution pores, and that the spatial distribution of the pores is highly heterogeneous. The average pore radius range, average throat radius range, and average coordination number range of micronmeter-sized pores are 2.09~3.42 μm, 1.32~2.19 μm, and 0.48~1.49, respectively. Restricted by the concentrated distribution of local anhydrite, the connectivity of micronmeter-sized pores develops well only in the anhydrite, showing negligible contribution to the overall reservoir connectivity. In contrast, nanometer-sized pores in the mixed siliciclastic-carbonate tight reservoirs are mainly intercrystalline pores in dolomite. The range of nanometer-sized pores diameters is mainly distributed in 1.73-31.47 nm. The pores have a smooth surface, simple structure, and relatively homogeneous spatial distribution. The dissolution of dolomite intercrystalline pores by acidic fluids increases the connectivity of the nanometer-sized pores. This paper presents genetic models for microscopic pore structures and connectivity of mixed siliciclastic-carbonate rocks, making possible the evaluation on the quality of the mixed siliciclastic-carbonate tight reservoirs.

1. Introduction

Mixed siliciclastic-carbonate deposits are defined as sediments consisting of both extrabasinal (e.g., epiclastic or terrigenous) and intrabasinal (autochthonous to parautochthonous) components, and they are an important type of continental sedimentary facies [1–3]. The sedimentary texture and mineral composition of mixed siliciclastic-carbonate tight reservoirs are by definition more varied than pure sandstones and carbonates [3–5]. There are 1.454 billion tons of recoverable oil in tight reservoirs in China, with more than 40% in mixed siliciclastic-carbonate tight reservoirs [2]. The huge resource potential has result in studies of the classification, depositional setting, and heterogeneity

of the mixed siliciclastic-carbonate rocks [6–13]. So far, many breakthroughs have been made on the classification and depositional setting of mixed siliciclastic-carbonate rocks [5, 9, 10, 12]. However, understanding the pore structure and connectivity of mixed siliciclastic-carbonate tight reservoirs, and the associated key controlling factors, is still lacking [14, 15].

Pore structure and pore connectivity are two important factors influencing the storage and flow capacity of tight reservoirs [16–19]. There have been numerous theoretical research on the micro- and nanometer-sized pore structures of tight sandstone reservoirs [18–22]. Due to effects caused by compaction and diagenesis, tight sandstone reservoirs are frequently featured by broad pore-sized distributions [17, 23], ranging from a few nanometers to tens of micronmeter, in addition to complex pore structures and poor pore throat connectivity [23–26]. In contrast, there are few studies of pore structure and connectivity mixed siliciclastic-carbonate tight reservoirs with complicated mineral compositions and diversified sedimentary textures. Determining the pore structures and their connectivity, as well as the intrinsic relationship between both the aspects of mixed siliciclastic-carbonate tight reservoirs, is key to understanding the heterogeneity in reservoirs quality.

The Yingxiongling Tectonic Belt is located in the western part of the Chaixi Depression in the Qaidam Basin. The petroleum resources are estimated to be 1.9 billion tons [27]. The cumulative proven petroleum reserves in the belt are ~500 million tons, accounting for 60% of the total reserves in the Qaidam Basin [27]. Mixed siliciclastic-carbonate tight reservoirs are characterized by complex mineral compositions, heterogeneity, which hampers the efficient development of these reservoirs [27]. In this study, thin section microscopy, X-ray diffraction, X-ray computed tomography, low pressure N_2 adsorption, and spontaneous inhibition were used to study the petrological properties, pore structure, and connectivity in the mixed siliciclastic-carbonate tight reservoirs of the upper member of the Xiaganchaigou Formation (E_3^2) in the Yingxi Area. Finally, a genetic model for the pore structure and connectivity at micrometer and nanometer scales has been established. This study provides a scientific basis for the evaluation of mixed siliciclastic-carbonate reservoirs.

2. Geological Settings

The Yingxi area is located in the western part of the Chaixi Depression in the Qaidam Basin (Figure 1(a)). Since the Cenozoic, the basin has been compressed from two directions by the Altun Mountain and the Kunlun Mountain, experiencing three stages of tectonic evolution in the process. This resulted in the formations of well-developed faults in the area and various other complex tectonic styles, such as Shizigou-Huatugou and Youyuangou, giving birth to a diverse tectonic framework altogether (Figure 1(b)) [28, 29]. The sedimentary process has been controlled by the process of regional tectonic evolution [30]. Under the arid paleoclimate, the depositional setting of the E_3^2 member underwent an initial salinization stage, the main salinization stage, and finally saline lake stage, successively (Figure 1(c)) [31, 32]. At the initial salinization stage, the basin formed a moderate-to-deep water depth lacustrine sedimentary environment. This was the stage where the main source rocks developed. At the intermediate stage, a saline lacustrine sedimentary environment dominated; as a result of a general decrease in sedimentation rates together with increased evaporation, the lake salinity generally increased, while the water depth changed from shallow nearshore to moderate-depth in a high-frequency oscillatory trend, combining into a considerably intensified development period for mixed siliciclastic-carbonate reservoirs. Finally, saline lake development, which featured the least active rate of supply from the sources and increased evaporation, leads to the sedimentary recycling characterized by the evaporation of lake water and drying out of the lake.

3. Samples and Methods

3.1. Samples and Sample Preparation. Eight samples of the mixed siliciclastic-carbonate rocks were collected from core taken from wells S220 and S41-6-1 in the upper member of Palaeogene Ganchaigou Formation. The sample number and the corresponding depths are shown in Table 1. Standard samples (cylinders with a length of 5 cm and a diameter of 2.5 cm) were drilled in the core. Afterwards, the samples were washed to remove residual oil in the standard samples, after which the samples were dried at 120°C for 24 h. Sample preparation is performed in the State Key Laboratory of China University of Petroleum (Beijing).

3.2. Thin Section Microscopy. 2 mm slices were cut from the top of each standard samples and ground into 0.3 mm sized thin section. The thin section was then impregnated under vacuum with blue epoxy to highlight the pore spaces. In addition, half of each thin section was stained with alizarin red S and K-ferricyanide to identify carbonate cementation. The samples were then observed with ZEISS Axioskop 40 optical microscope in the State Key Laboratory of China University of Petroleum (Beijing) under reflected light and transmitted light (polarized light), in order to determine the clastic constituents and structure, as well as the type of cement in the reservoir [17]. The detailed information of samples are list in Table 1.

3.3. X-Ray Diffraction (XRD). A chip of about 5 g was taken from each sample and then crushed to particles about 48 μm. At room temperature (25°C), XRD analysis was performed with an Ultima IV automatic XRD analyzer (Rigaku, Tokyo, Japan) in the State Key Laboratory of China University of Petroleum (Beijing). The Joint Committee on Powder Diffraction Standards, International Diffraction Data Center (JCPDS-ICDD) was founded in 1941 to produce a primary reference of X-ray powder diffraction data. During the experiment, the X-ray diffraction spectrum mainly refers to the database from JCPDS-ICDD to identify the mineral components in the mixed siliciclastic-carbonate rocks. The detailed information of samples are list in Table 1.

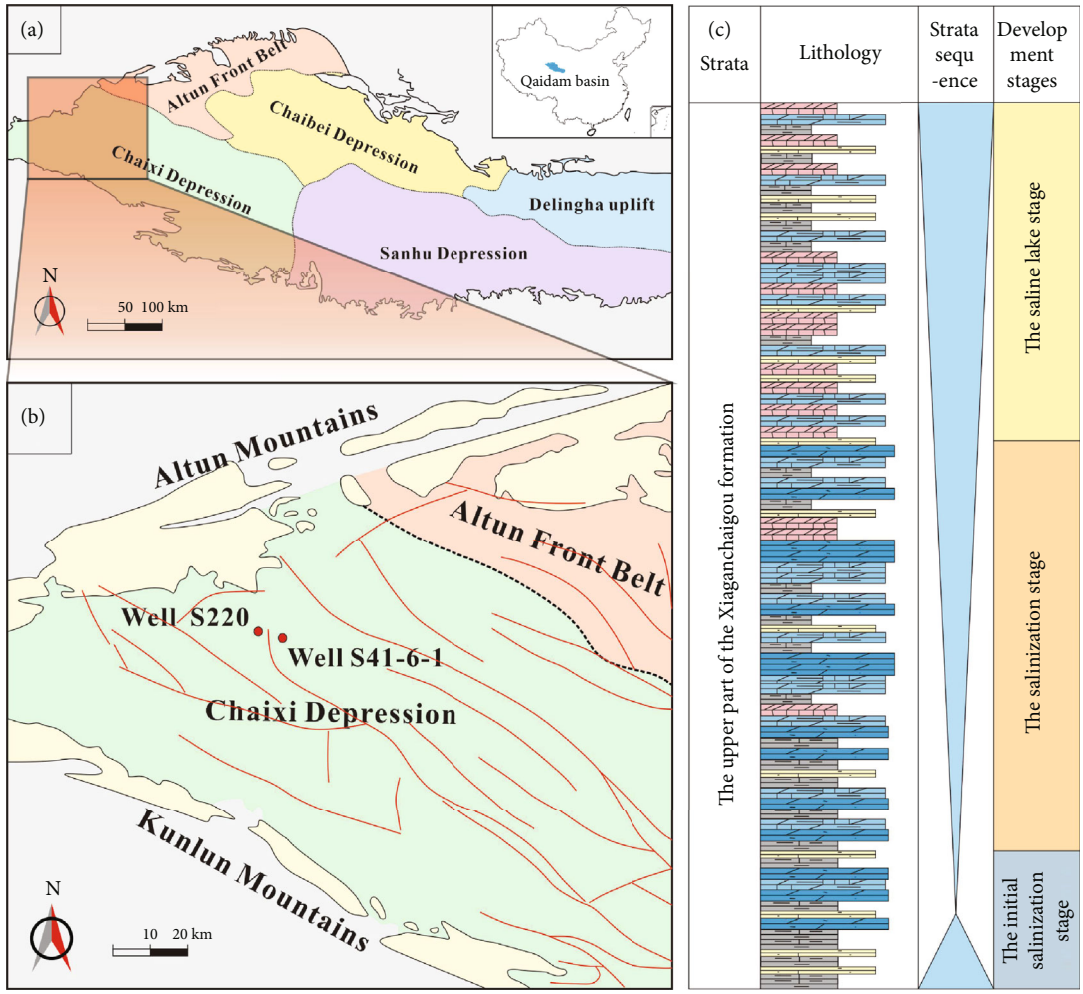

Figure 1: (a) Map showing the tectonic subdivisions of the Qaidam Basin in the northwestern China and the location of research area (indicated by the box). (b) Map showing the location and Chaixi Depression and targeted boreholes. (c) Vertical profile of the Upper member of Palaeogene Xiaganchaigou Formation showing lithology and sequences.

Table 1: Details of tight reservoir samples collected from the E_3^2 member of Xiaganchaigou Formation, Qaidam Basin.

Sample ID	Well ID	Formation	Reservoir type	Depth (m)
MSCSs-1	S41-6-1	E_3^2	LDR	3863.11
MSCSs-2	S41-6-1	E_3^2	LDR	3862.22
MSCSs-3	S41-6-1	E_3^2	LDR	3863.26
MSCSs-4	S220	E_3^2	LDR	4309.97
MSCSs-5	S41-6-1	E_3^2	SCR	3864.81
MSCSs-6	S220	E_3^2	SCR	3944.24
MSCSs-7	S220	E_3^2	MSCR	4317.26
MSCSs-8	S220	E_3^2	MSCR	4312.14

LDR: rocks containing more than 50% carbonate minerals; SCR: rocks containing more than 50% siliceous clastic minerals; MSCR: rocks containing less than 50% of any mineral.

3.4. X-Ray Computed Tomography (CT). A cylindrical sample with a diameter of 0.25 cm was drilled from each standard sample. Zeiss Xradia Versa-510 micro-CT in the State Key Laboratory of China University of Petroleum (Beijing) was used to scan the sample at a scan resolution of 1 μm. The scan voltage and current were set to 120 keV and 10 μA, respectively, to ensure good X-ray penetration. 991 two-dimensional (2D) tomographic images were obtained via CT scan per sample, and these were reconstructed into three-dimensional (3D) gray images using a back projection algorithm [33–35]. The pore network model (PNM) established based on a maximum spherical algorithm was coupled with Avizo Software Kit to perform grayscale segmentation of the reconstructed images [33–35]. The pore system was differentiated from the rock matrix based on the difference in X-ray attenuation observed from the penetration of materials with varying densities [36]. Finally, the number, volume, and radius of pores and throats could be obtained from the recorded statistics [37]. The detailed information of samples are list in Table 1.

3.5. Low Pressure N_2 Adsorption. About 1 ~ 2 g of powder sample (187.5 μm) was prepared from the standard core. The sample was degassed at 110°C under a vacuum for about 14 h to remove the adsorbed moisture and volatile substances. A Micromeritics® Tristar II 3020 surface area

analyzer in the State Key Laboratory of China University of Petroleum (Beijing) was used for low pressure (<0.127 MPa) N_2 adsorption analysis. The relative pressure (P/P_0) range of N_2 adsorption was set to 0.001 to 0.995. The adsorption isotherm curve was then automatically generated using the built-in device software based on the desired adsorption theories [38–41]. In addition, the surface area, pore volume, and pore size distribution were calculated [17, 42]. The detailed information of samples are list in Table 1.

3.6. Spontaneous Imbibition (SI). SI is a capillary force controlled process, in which the nonwetting phase is spontaneously displaced by the wetting phase only via capillary suction. A cube with a side length of 1 cm was prepared from the standard sample. Afterwards, all sides (except for the top and the bottom) were coated with fast curing clear epoxy resin to generate absorption only in a vertical direction. Water and n-decane were used to displace the nonwetting phase air. In order to ensure that a sample was at irreducible water saturation initially, all samples were dried at 60°C (140°F) for at least 48 h, after which the imbibition experiment was carried out. SI analyzer was used for spontaneous imbibition experiments in the State Key Laboratory of China University of Petroleum (Beijing). The schematic diagram, experimental procedure, and data processing method of the SI experiment were as described in detail by Gao and Hu [43]. The detailed information of samples are list in Table 1.

4. Results

4.1. Petrologic Properties and Classification of Mixed Siliciclastic-Carbonate Tight Reservoirs

4.1.1. Petrologic Properties. The XRD data for the samples (Figure 2) show that the minerals found in the eight samples are mainly siliceous clastic minerals (quartz, potassium feldspar, plagioclase), carbonate minerals (calcite, iron dolomite, dolomite), sulfate minerals (gypsum, glauberite, anhydrite), clay minerals, a small amount of other minerals (pyrite, stone salt, and siderite), etc. The samples can be generally characterized by the presence of significant differences in the contents of various mineral types, as well as the significant discrepancies in the contents of the same mineral in different samples (Figure 2). The distribution of mineral types is also complex, highlighting the characteristic of mixed siliciclastic-carbonate deposition as a whole. Microscopically, anhydrite was cemented severely, but the innner of anhydrite was obviously dissolved (Figures 3(a) and 3(b)). Dolomite minerals were mainly structurally composed of micrite or microcrystals and were mixed with siliceous clastic particles (Figures 3(c) and 3(d)).

4.1.2. Classification of Mixed Siliciclastic-Carbonate Tight Reservoirs. Based on the relative minerals contents (clay, carbonate, siliciclastic, and sulfate minerals), the samples are classified into three types (siliceous clastic rocks, lime-dolostone rocks, mixed siliciclastic-carbonate rocks) [5, 44]. Rocks with a relative content of terrestrial clastic minerals greater than 50% are defined as siliceous clastic rocks (SCR), while those that hold more than 50% of carbonate are called lime-dolostone rocks (LDR). Rocks with minerals relative content of each type below 50% are called mixed siliciclastic-carbonate rocks (MSCR). Reservoir classification is shown in Table 1.

4.2. Pore Structure and Connectivity of Mixed Siliciclastic-Carbonate Tight Reservoirs

4.2.1. Characterization of Connectivity and Pore Structures by CT. The eight samples were scanned by CT. The images of 3D pore throat spatial distribution and the PNM of the pore system in the mixed siliciclastic-carbonate tight reservoirs obtained from the grayscale segmentation processing are shown in Figure 4. The images of 3D pore throat spatial distribution were then superimposed and marked with colors. The pore sizes and connectivity of each sample can be directly observed (Figure 4). In adjacent regions, the same color means implies connected pores, while different colors indicate isolated or disconnected pores [37]. It is lesser that the volume covered by the pores of the same color (Figures 4(a), 4(c), 4(e), 4(g), 4(i), 4(k), 4(m), and 4(o)). The overall connectivity of the pore system is poorer. However, in areas where pores are locally concentrated, the connectivity of the local pore system is the better (Figures 4(a), 4(c), 4(e), 4(g), 4(i), 4(k), 4(m), and 4(o)). Furthermore, significant differences in the spatial distribution of the pore system were also found in the three types of the mixed siliciclastic-carbonate tight reservoirs. The spatial distribution of pore of lime-dolostone tight reservoirs is relatively homogeneous (Figures 4(a)–4(h)), while the heterogeneities of the spatial distributions of pore in the tight reservoirs of siliceous clastic rocks (Figures 4(i)–4(l)) and mixed siliciclastic-carbonate rocks (Figures 4(m)–4(p)) are high.

The distribution of the pore and throat radius of the eight samples calculated with the PNM [33–35] is shown in Figure 5 and Table 2. The X ray CT method could not characterize the nanometer-sized pores due to resolution limitations. The pore radius values fall between 1 and 40 μm, while the throat radius values plot in the range of 1 ~ 25 μm. The pore radius in Figure 5(a) shows two overlapping peaks. The first peak is between 3.5 and 5 μm. These pores make up the main micrometer scale pore space in the mixed siliciclastic-carbonate tight reservoirs. The second peak is between 7.5 and 9 μm. The throat radius peaks are concentrated between 4 and 5 μm (Figure 5(b)). Different types of tight reservoirs also present similar pores and throat combination characteristics. The average pore radius range, average throat radius range, and average coordination number range are 2.09~3.42 μm, 1.32~2.19 μm, and 0.48~1.49, respectively (Table 2).

4.2.2. Characterization of Pore Structure by N_2 Adsorption. Nanopore that cannot be determined by X-ray micro-CT can be measured by the nitrogen adsorption method [17]. The nanopore size distribution curves of the eight samples are shown in Figure 6. These curves were derived using the BJH model [39, 40]. Significant differences in pore size distributions as a function of lithology can be observed. The

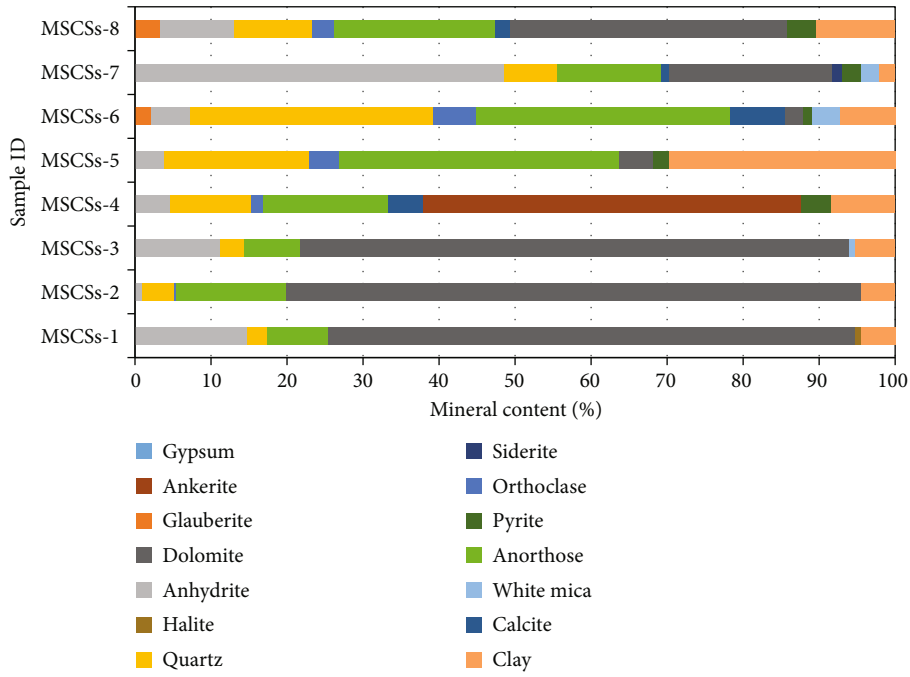

Figure 2: Mineral composition of the eight samples collected from the E_3^2 member of the Xiaganchaigou Formation.

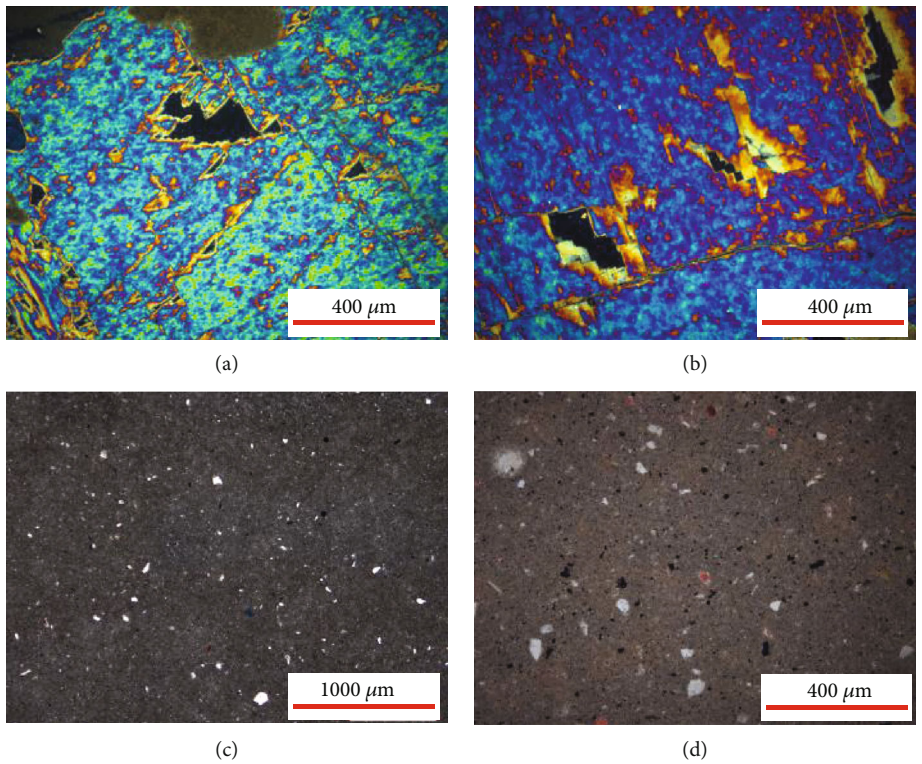

Figure 3: Microscopic observation of the Palaeogene Xiaganchaigou Formation samples from Qaidam Basin. Massive development of gypsum cements and remaining of numerous microscale dissolution pores: (a) 4312.14 m and (b) 4317.26 m. Mixed sendimentation of micrite or microcrystal dolomite and siliceous clastic particles: (c) 3864.81 m and (d) 3863.11 m.

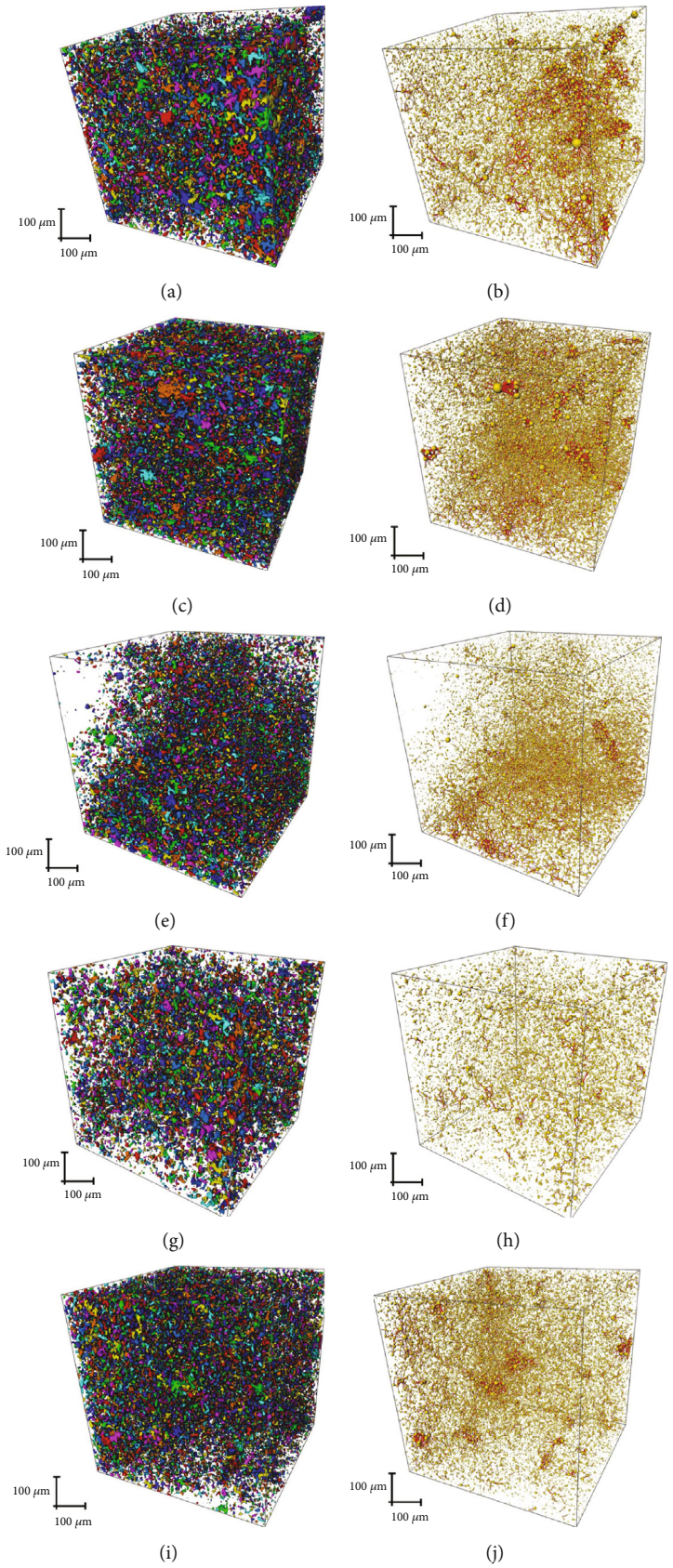

Figure 4: Continued.

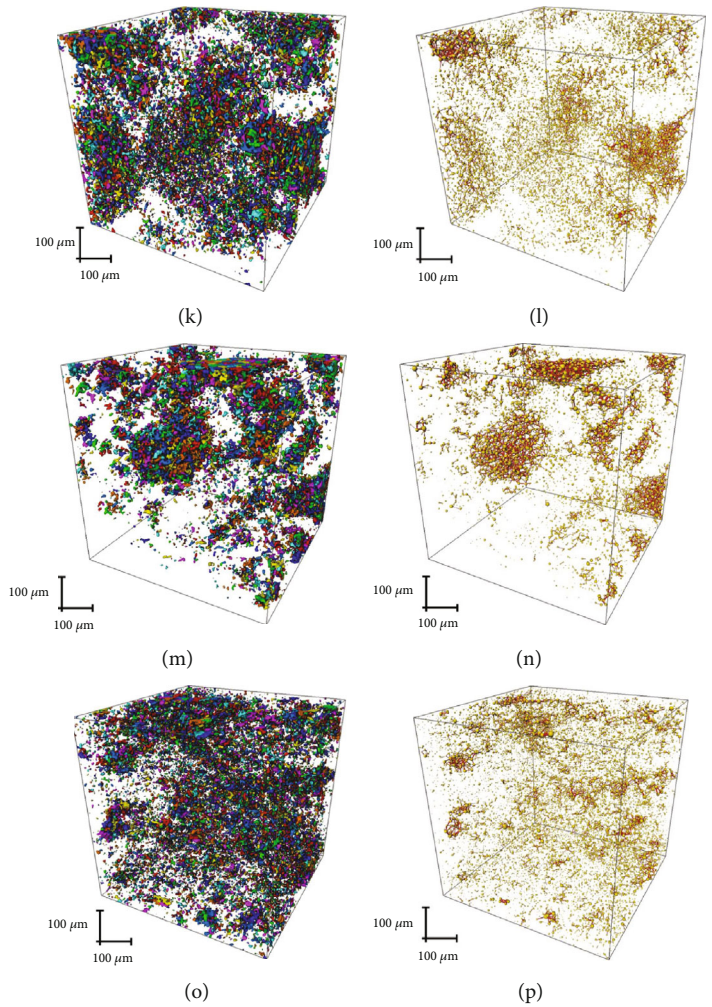

Figure 4: 3D micro-CT imaging on the pore throat networks of tight reservoir samples from the Upper member of Palaeogene Xiaganchaigou Formation, Qaidam Basin. (a) MSCSs-1. (b) MSCSs-1. (c) MSCSs-2. (d) MSCSs-2. (e) MSCSs-3. (f) MSCSs-3. (g) MSCSs-4. (g) MSCSs-4. (i) MSCSs-5. (j) MSCSs-5. (k) MSCSs-6. (l) MSCSs-6. (m) MSCSs-7. (n) MSCSs-7. (o) MSCSs-8. (p) MSCSs-8.

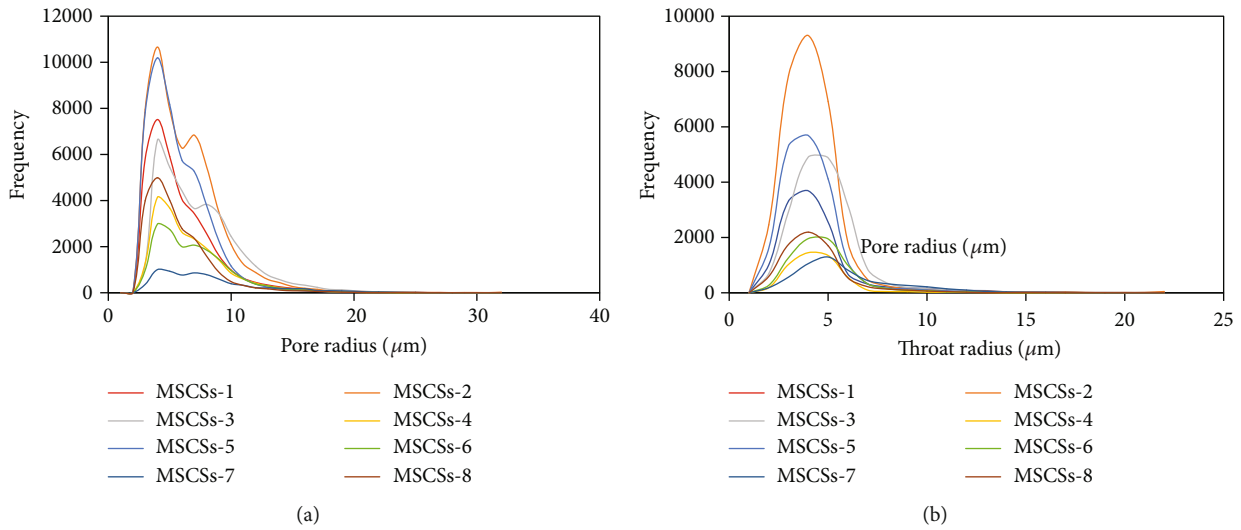

Figure 5: Pore throat size distribution of tight reservoir samples from the upper member of Palaeogene Xiaganchaigou Formation, Qaidam Basin.

Table 2: Pore structure parameters of the Palaeogene Xiaganchaigou Formation samples measured by 3D micro-CT imaging.

Sample ID	Reservoir type	Average pore radius (μm)	Average throat radius (μm)	Average coordination number
MSCSs-1	LDR	2.225	1.522	0.733
MSCSs-2	LDR	2.384	1.367	1.086
MSCSs-3	LDR	2.948	1.651	0.998
MSCSs-4	LDR	2.570	1.486	0.477
MSCSs-5	SCR	2.091	1.320	0.813
MSCSs-6	SCR	2.752	1.629	0.845
MSCSs-7	MSCR	3.420	2.190	1.485
MSCSs-8	MSCR	2.089	1.435	0.663

range of pore diameters is 2-100 nm, while the pore diameter distributions of most samples show a bimodal pattern (Figures 6(a), 6(d), and 6(e)–6(h)). The first peak appears between 1.73 and 3.07 nm and the other between 5.61 and 31.47 nm. The distribution curves of the pore size of the remaining samples show a unimodal pattern (Figures 6(b) and 6(c)), with peaks tending to occur between 2.7027 and 2.8617 nm.

The fractal fitted curves of the eight samples can be divided into two different linear segments, corresponding to relative pressures (P/P_0) of 0-0.45 and 0.45-1 (Figure 7). Satisfactory linear correlation between segments indicates that the two segments have different gas adsorption behaviors. Therefore, considering the differences in the gas adsorption behavior, the fractal dimensions should also be separately defined in two parts [42]. At the low pressure segment ($P/P_{0=}0-0.45$), van der Waals' force is the main force of gas adsorption responsible for the monolayer adsorption. At this point, the fractal dimension can describe the fractal characteristics of pore surface expressed as D_1 [38–40]. As the pressure increases ($P/P_{0=}0.45-1$), the gas adsorption is transformed into multilayer adsorption mainly via capillary condensation. At this point, the fractal dimension can describe the fractal characteristics of pore structure expressed as D_2 [38–40].

As shown in Table 3, the BJH total pore volume (BJH TPV), BJH average pore diameter (BJH APD), and fractal dimensions (D_1 and D_2) have been obtained from the low pressure N_2 adsorption isotherms analysis. LDR samples have relatively higher values of BJH TPV and D_1. BJH TPV falls within the range of 0.003533~0.020521 $cm^3/(g{\cdot}nm)$, averaging 0.011569 $cm^3/(g{\cdot}nm)$, while BJH APD falls between 18.6645 and 21.8562 nm, averaging 20.3105 nm. D_1 is within the range 2.4274~2.5537, averaging 2.5084, while D_2 is within the range of 2.2331~2.5073, averaging 2.4149. The SCR samples have relatively higher BJH APD and lower BJH TPV values. The MSCR samples have relatively higher value of D_2.

4.2.3. Characterization of Connectivity of Micronano Pores by SI. The SI experiments use water and n-decane and showed that samples were unstable when they settled into the fluid in the first 30 seconds or so, resulting in fluctuations in weight (Figure 8). After the initial stage of instability, the cumulative height of the fluid imbibed was linearly proportional to the time (Figure 8). The gradient of the logarithmic relationship between the cumulative SI height and the time is shown in Table 4, and this represents the connectivity of hydrophilic (from the water experiments) and lipophilic (from the n-decane experiments) pores. According to the Handy equation and imbibition theory [45, 46], if an imbibition slope of 0.5 is obtained, porous media have in theory good pore connectivity for the fluid used, while lower slopes (<0.5) may indicate a low pore connectivity to the fluid [43].

The slope for imbibition of n-decane is always greater than that for water, indicating that the connectivity of oil-wetting pores in the samples is superior to that of hydrophilic pores. For the four LDR samples with relatively higher content of carbonate minerals, the spontaneous imbibition slope of n-decane is greater than the theoretical value 0.5, with a mean of 0.583, indicating that the connectivity of oil-wetting pores is good. For the SCR and MSCR samples with relatively lower content of carbonate minerals, the average value of the slope of n-decane is 0.49 and 0.47, respectively, both of which are close to the theoretical value 0.5. Although the spontaneous imbibition slope is lower than that in LDR samples, it also shows favorable connectivity of oil-wetting pores. The connectivity of hydrophilic pores varies widely among different types of samples for all samples. The connectivity of hydrophilic pores in LDR samples is low, showing range of values from 0.242 to 0.394. There is a great difference in the connectivity of hydrophilic pores in SCR and MSCR samples, with slope values of 0.255 and 0.476 and 0.164 and 0.423, respectively.

5. Discussion

5.1. The Influence of Mineral Composition on the Structure and Connectivity of Micrometer Scale Pores in Mixed Siliciclastic-Carbonate Tight Reservoirs. At the penecontemporaneous stage, part of the E_3^2 stratum is above water and is affected by the leaching of atmospheric fresh water [47]. Since the Yingxi Area is the $CaCO_3$-$CaSO_4$-H_2O-CO_2 diagenetic system, the atmospheric fresh water demonstrated higher proclivity to dissolve gypsum cements or crystals to form dissolution pores [47, 48]. At the diagenetic stage, the gypsum gradually dehydrated into anhydrite [47, 49]. Afterwards, the dissolution pores formed at the penecontemporaneous stage were retained in anhydrite minerals (Figures 3(a) and 3(b)). As a result, the higher the anhydrite content, the greater the average pore radius, average throat radius, and coordination number (Figures 9(a), 9(d), and 9(g)). Therefore, the dissolution and dehydration conversion

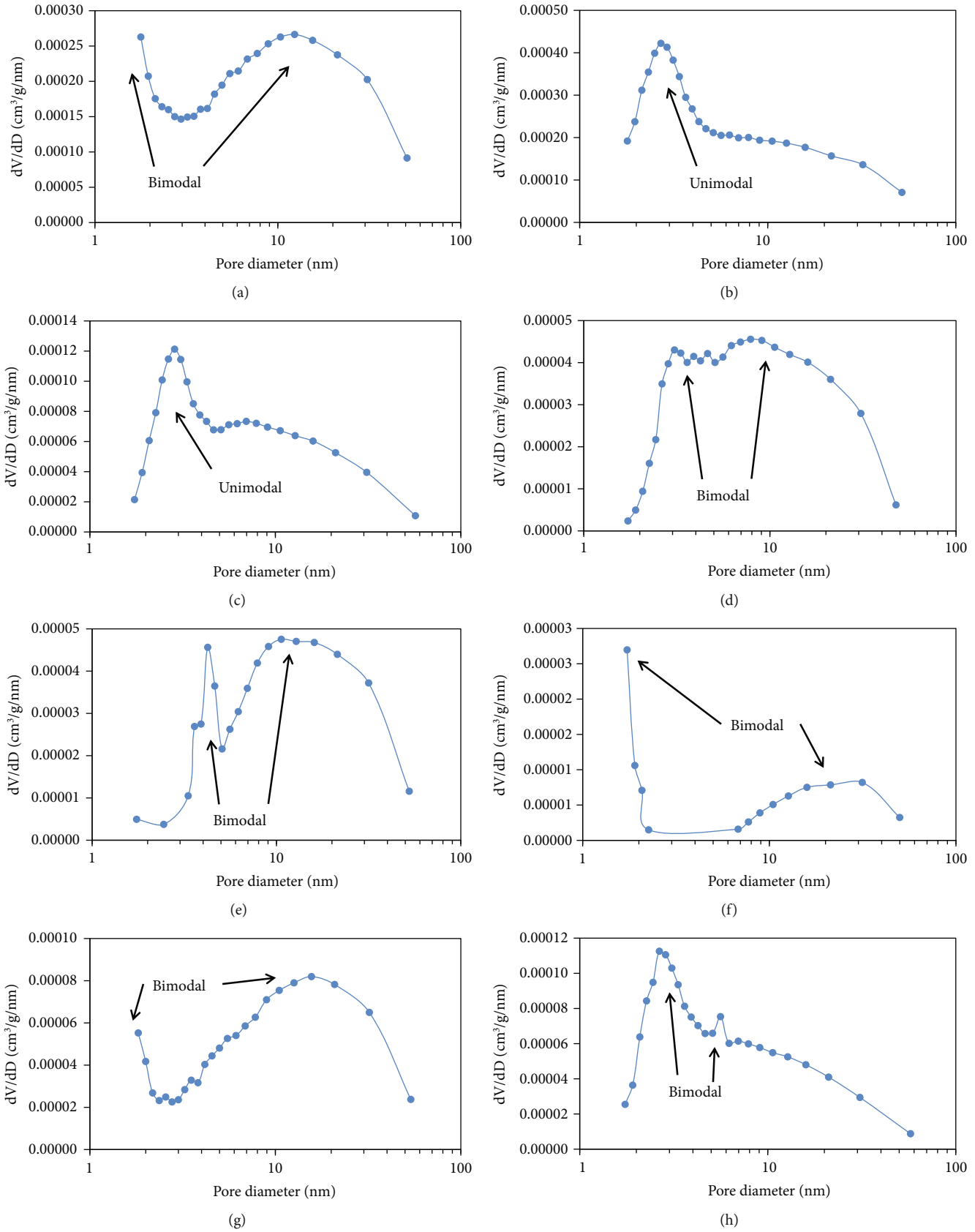

Figure 6: Pore-sized distribution of tight reservoir samples from the Palaeogene Xiaganchaigou Formation samples measured by low pressure N_2 adsorption. (a) MSCSs-1. (b) MSCSs-2. (c) MSCSs-3. (d) MSCSs-4. (e) MSCSs-5. (f) MSCSs-6. (g) MSCSs-7. (h) MSCSs-8.

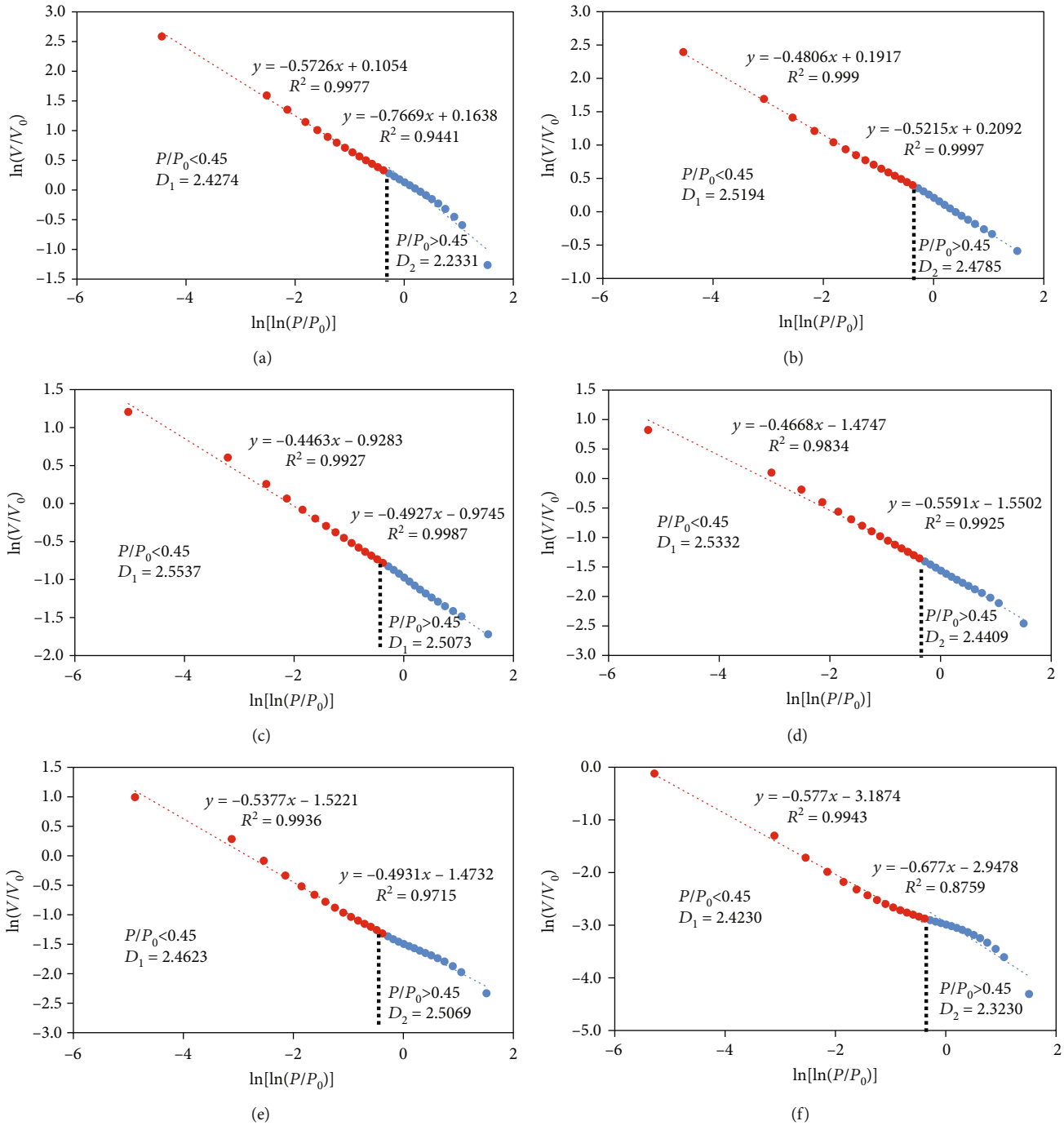

Figure 7: Continued.

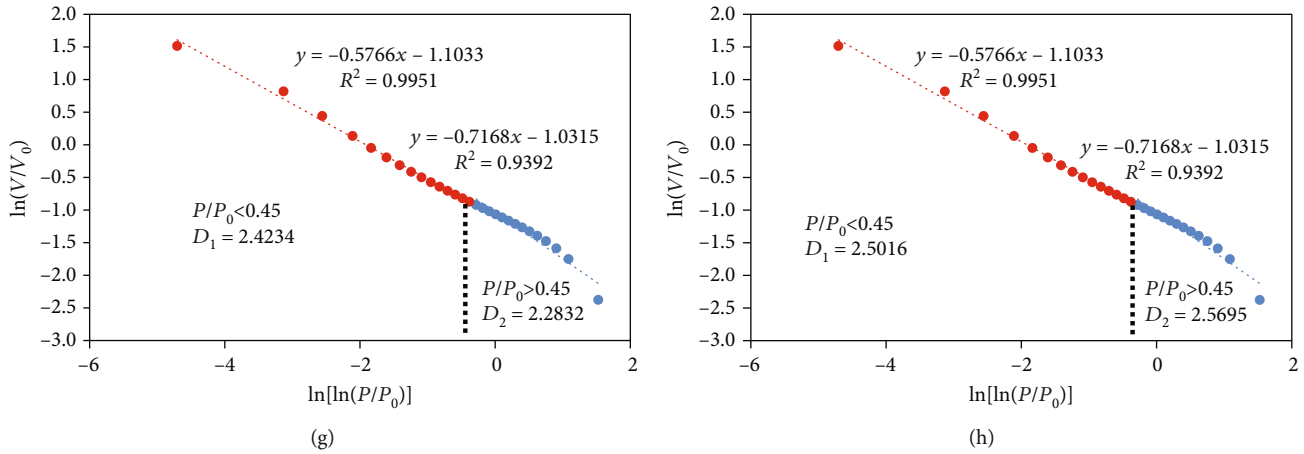

Figure 7: Pore fractal characteristics of the eight samples. (a) MSCSs-1. (b) MSCSs-2. (c) MSCSs-3. (d MSCSs-4. (e) MSCSs-5. (f) MSCSs-6. (g) MSCSs-7. (h) MSCSs-8.

Table 3: Pore structure parameters of the eight samples measured by low pressure N_2 adsorption.

Sample ID	Reservoir type	BJH TPV (cm^3/g)	BJH APD (nm)	D_1	D_2
MSCSs-1	LDR	0.020521	21.856200	2.4274	2.2331
MSCSs-2	LDR	0.017060	18.664500	2.5194	2.4785
MSCSs-3	LDR	0.005161	18.894500	2.5537	2.5073
MSCSs-4	LDR	0.003533	21.826900	2.5332	2.4409
MSCSs-5	SCR	0.004156	26.547600	2.4623	2.5069
MSCSs-6	SCR	0.001375	34.995100	2.4230	2.3230
MSCSs-7	MSCR	0.007042	25.639500	2.4234	2.2832
MSCSs-8	MSCR	0.003725	16.384000	2.5016	2.5695

of gypsum are the main contributors of micronmeter-sized pores and throats. Nevertheless, the contribution of the pore and throat system in the anhydrite to the reservoir is extremely limited. On the one hand, as restricted by the spatial distribution of anhydrite, the spatial distribution of pores in mixed siliciclastic-carbonate tight reservoirs with relatively developed anhydrite is highly heterogeneous (Figures 4(m)–4(p)); on the other hand, the cementation of anhydrite at the diagenetic stage blocks the connection between the pore network in anhydrite and the outside world. As a result, numerous developed connected pores in anhydrite minerals fail to improve the overall connectivity in the reservoir. Clay minerals are common cements and interstitial materials in reservoirs and often block reservoir space [50]. Accordingly, the higher the content of clay minerals, the smaller the average pore radius, the average throat radius, and the coordination number (Figures 9(c), 9(f), and 9(i)). Therefore, clay minerals are the main destroyer of micronmeter-sized pores and throats. Since the duration of the sedimentary and diagenetic processes of dolomite is short, the main structures are either micrite or microcrystal (Figures 3(c) and 3(d)). The intercrystalline pores and their later intercrystal dissolution pores are mainly nanometer scale [51]. Therefore, the dolomite content has no control over the structure and connectivity of micro pores (Figures 9(b), 9(e), and 9(h)).

5.2. The Influence of Mineral Composition on the Structure of Nanometer Scale Pores in Mixed Siliciclastic-Carbonate Tight Reservoirs. The nanometer-sized pores in the eight samples are mainly controlled by the dolomite content (Figures 10(b) and 10(e)), while anhydrite content and the content of clay minerals have no obvious control effect on nanometer-sized pores (Figures 10(a), 10(c), 10(d), and 10(f)). The volume of nanometer-sized pores increases with the increase of dolomite content (Figure 10(b)). At the penecontemporaneous stage, with the intense water evaporation, the crystallization and differentiation of sulfate minerals occur [47]. As a result, Mg^{2+} is enriched in large quantities. Under gravity, the bittern in which Mg^{2+} is enriched permeates below the formation; and metasomatism occurs between bittern and calcite to form dolomite [47, 51, 52]. Numerous developed intercrystalline pores in dolomite minerals are mainly formed by the volume shrinkage caused by the replacement of Mg^{2+} with smaller radius to Ga^{2+} with larger radius [51–53]. The high mud content in carbonatites results in the small scale of intercrystalline pores in dolomite and the disconnection between pore. Therefore, the more developed the dolomite, the larger proportion of pores with smaller pores and the smaller the average of the pore radius in the reservoir (Figure 10(e)). Meanwhile, the dolomite formed earlier has compaction pressure solubility resistance, inhibiting the damage to the reservoir caused by compaction and pressure dissolution [53]. Intercrystalline pores are generally preserved in this way.

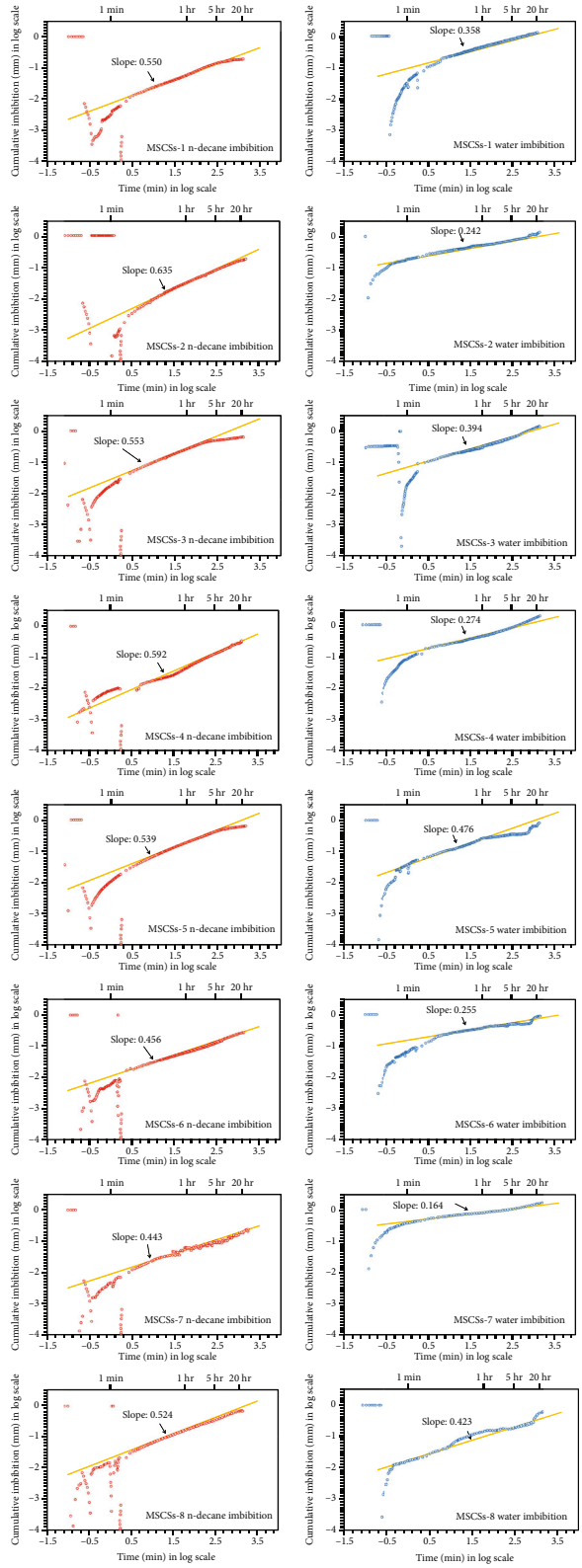

Figure 8: Connectivity of oil-wetting pores and water pores measured by spontaneous imbibition.

Meanwhile, the fractal dimension was used to analyze the relation between the mineral composition and pore structure in the mixed siliciclastic-carbonate tight reservoirs. As shown in Figures 10(g) and 10(j), both D_1 and D_2 are negatively correlated to the anhydrite content, indicating that the increase of the anhydrite content may lead to simpler pore structure and smoother pore surface. This is consistent with previous findings [49, 54]. As shown in

Table 4: Pore connectivity parameters of the eight samples measured by spontaneous imbibition.

Sample ID	Reservoir type	Fluid used	Imbibition slope
MSCSs-1	LDR	n-Decane	0.550
		Water	0.358
MSCSs-2	LDR	n-Decane	0.635
		Water	0.242
MSCSs-3	LDR	n-Decane	0.553
		Water	0.394
MSCSs-4	LDR	n-Decane	0.592
		Water	0.274
MSCSs-5	SCR	n-Decane	0.539
		Water	0.476
MSCSs-6	SCR	n-Decane	0.456
		Water	0.255
MSCSs-7	MSCR	n-Decane	0.443
		Water	0.164
MSCSs-8	MSCR	n-Decane	0.524
		Water	0.423

*The density of water is 1.0 g/cm^3, and the viscosity of water is 1.002 mPa-sec; the density of n-decane is 0.73 g/cm^3, and the viscosity of n-decane is 0.84 mPa-sec.

Figures 10(h) and 10(k), D_1 is positively correlated to the dolomite content, while the dolomite content have no obvious control effect on D_2. In the process of dolomitization, polyhedral pores are transformed into tetrahedral pores [55]. In consequence, intercrystalline pores with a smooth surface appear as dolomite crystals increase. The content of clay minerals partly controls the complexity of the nanopores structure [56]. Compared with other minerals, clay minerals have more complicated chemical structure. Most pores in clay minerals are of a triangular, serrated, or other irregular shape. In consequence, the pore network becomes more complicated. D_2 is positively correlated to clay minerals (Figure 10(l)), indicating that the increase of the content of clay minerals has made the pore structure more complex. Clay minerals have no correlation with D_1 (Figure 10(i)).

5.3. The Influence of Mineral Composition on Connectivity of Pores in Mixed Siliciclastic-Carbonate Tight Reservoirs. Unlike conventional reservoirs, the mineral composition of mixed siliciclastic-carbonate tight reservoirs is more complicated [3–5]. Moreover, the wettability of different minerals results in different pore connectivity of the reservoir to different fluids [43]. According to the statistical results, the strong cementation of anhydrite destroys the connectivity of both oil-wetting and hydrophilic pores in the reservoir (Figures 11(a) and 11(d)). Dolomite is a lipophilic mineral and a main contributor to the connectivity of oil-wetting pores in the reservoir (Figure 11(b)). Clay minerals are hydrophilic minerals and are the main contributors to the connectivity of hydrophilic pores in the reservoir (Figure 11(f)).

The precipitation of sulfate minerals occurred twice in the sediments [47]. The first precipitation occurs at the penecontemporaneous stage. The lake water is gradually salinized with the evaporation and concentration of the water in the lake basin. The sulfate mineral components enter a saturated state, and gypsum begins to precipitate and fill between clastic grains and between clastic grains in carbonates. The second precipitation occurs at the diagenetic stage. The gypsum gradually dehydrates into anhydrite due to the increase of formation temperature and pressure. The anhydrite is cemented in the dissolution pores in gypsum and the intercrystalline pores in dolomite minerals. Therefore, the spontaneous imbibition slope of both n-decane and water decreases with the increase of the anhydrite content (Figures 11(a) and 11(d)), and the connectivity of both oil-wetting and hydrophilic pores is broken.

The dissolution of minerals by organic acids is of great significance for the connectivity of the reservoir [57]. The source rocks in the Yingxi area reached the peak of oil generation in the Pliocene Epoch [58]. The acid fluid produced by the hydrocarbon generation and expulsion from organic matter can make the intercrystalline pores in the dolomite minerals formed at the penecontemporaneous stage transform into intercrystalline dissolution pores [51, 59]. In carbonatites, the mud content is high; the intercrystalline scale between minerals is small, and most pores are isolated ones. The large-scale development of intercrystalline dissolution pores causes a slight increase in the pore size and passivation of edges, which improve the connectivity of intercrystalline pores and the reservoir effectiveness [59]. A great number of the intercrystalline dissolution pores formed by the dissolution by organic acids can be preserved for they are formed late and protected by hydrocarbon fluid. Therefore, the spontaneous imbibition slope of n-decane increases with the increase of dolomite content, and the connectivity of oil-wetting pores is improved (Figure 11(b)), but content of clay minerals and the spontaneous imbibition slope of n-decane are not correlated (Figure 11(c)).

The clay minerals in the upper member of Xiaganchaigou Formation, Oligocene, Yingxi Area, mainly are chlorite, illite, and illite-smectite mixed layer at the B substage of the diagenetic stage [58]. Previous studies have shown that for reservoirs with high illite-smectite mixed-layer content, the water-rock interaction optimizes the connected hydrophilic pore system, resulting in high water absorption capacity [43]. Therefore, the spontaneous imbibition slope of water increases with the increase of the content of clay minerals, and the connectivity of hydrophilic pores is improved (Figure 11(f)), but dolomite content and the spontaneous imbibition slope of water are not correlated (Figure 11(e)).

5.4. Genetic Model for Pore Structure and Connectivity of Mixed Siliciclastic-Carbonate Tight Reservoirs and Reservoir Evaluation. Agenetic model for the pore structure and connectivity of mixed siliciclastic-carbonate tight reservoirs has been established on the basis of the above discussion of the petrologic, pore structure, and pore connectivity

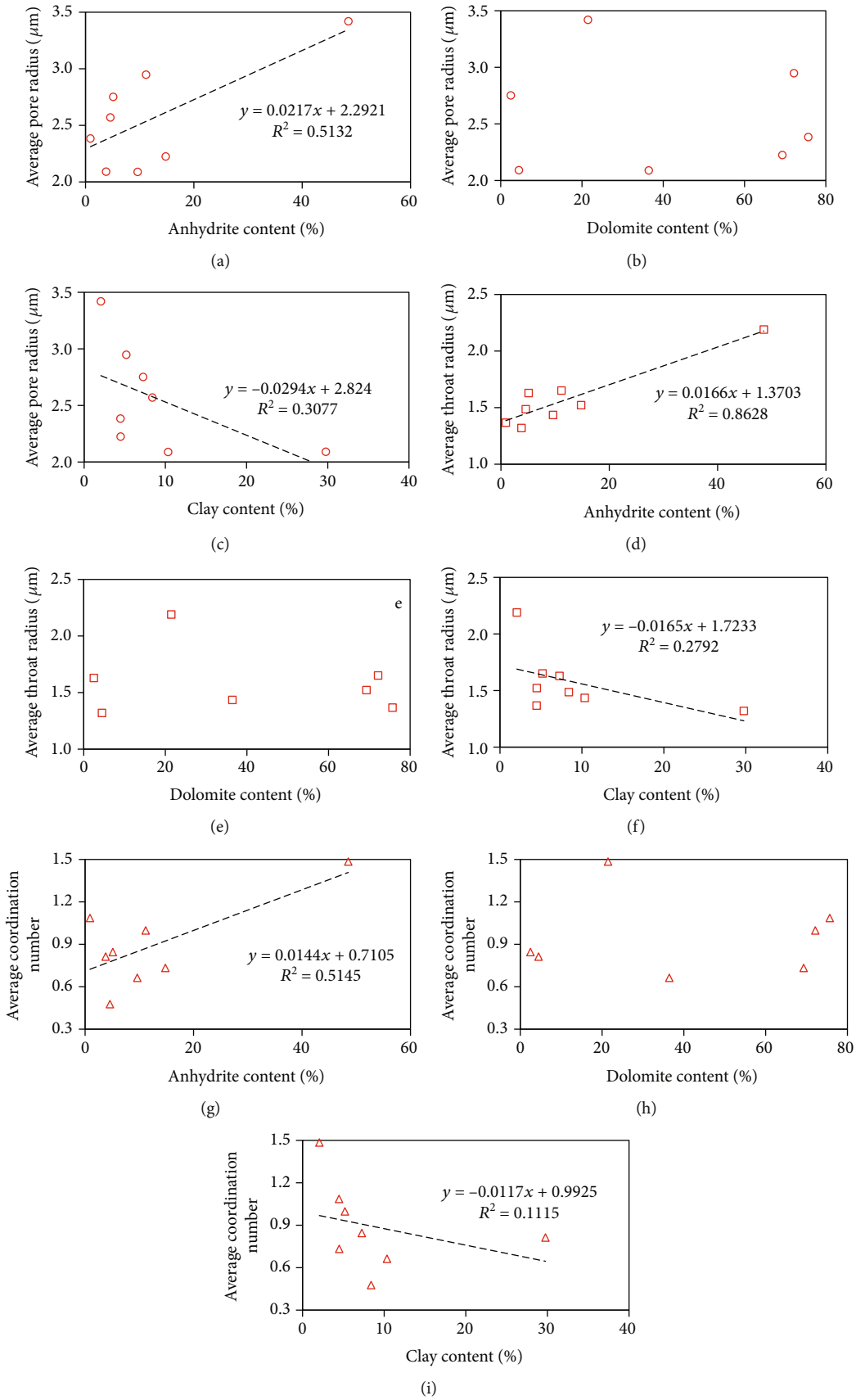

Figure 9: Crossplots of 3D CT parameters and mineral compositions of the eight samples.

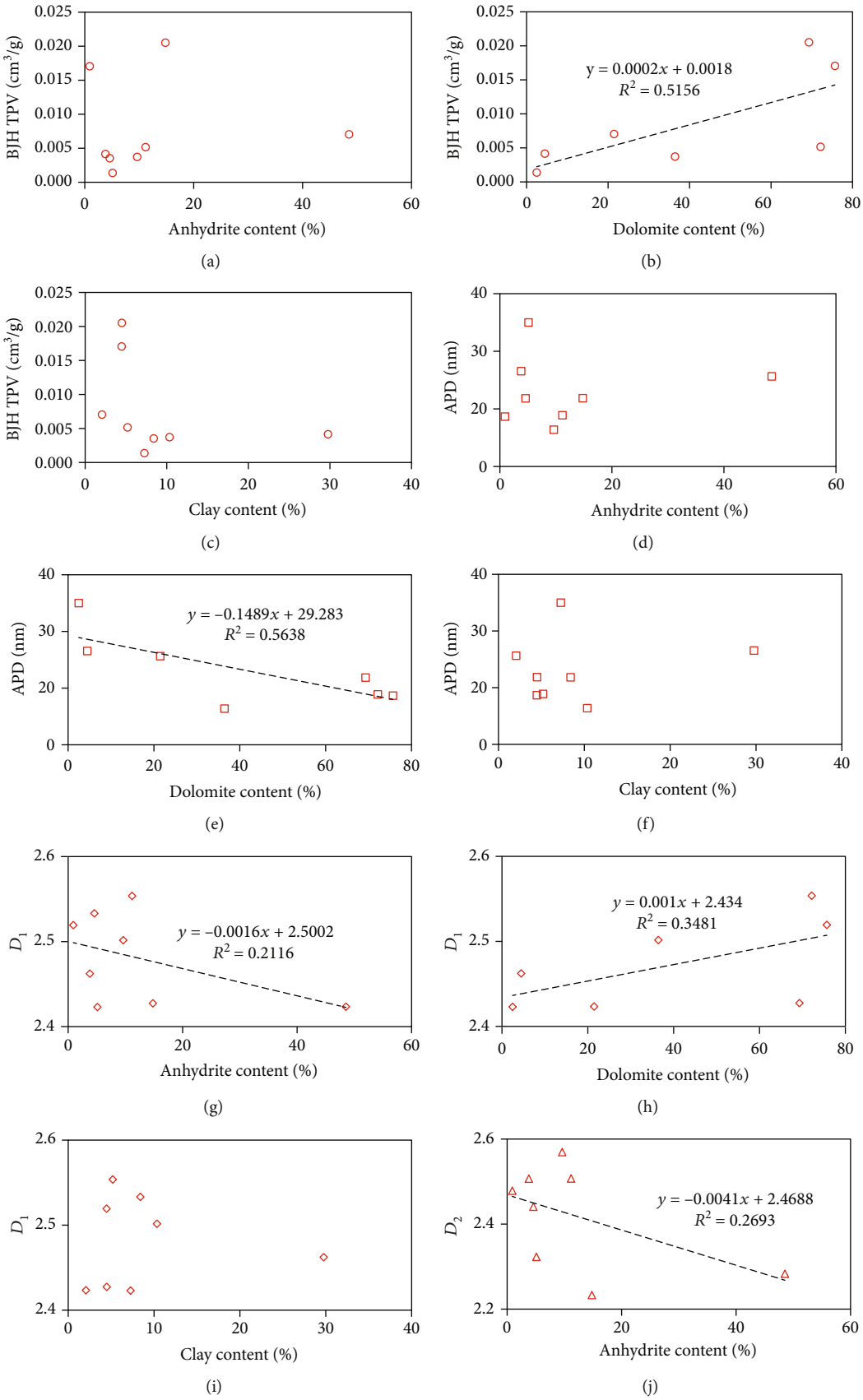

Figure 10: Continued.

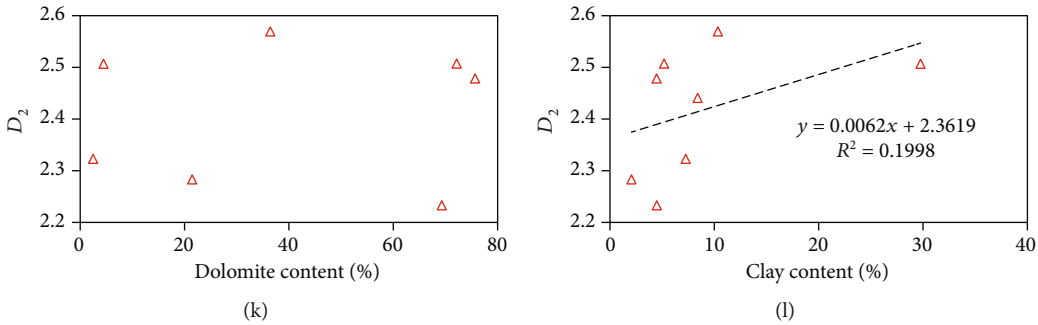

Figure 10: Crossplots of N_2 adsorption parameters and mineral compositions of the Palaeogene Xiaganchaigou Formation samples from Qaidam Basin.

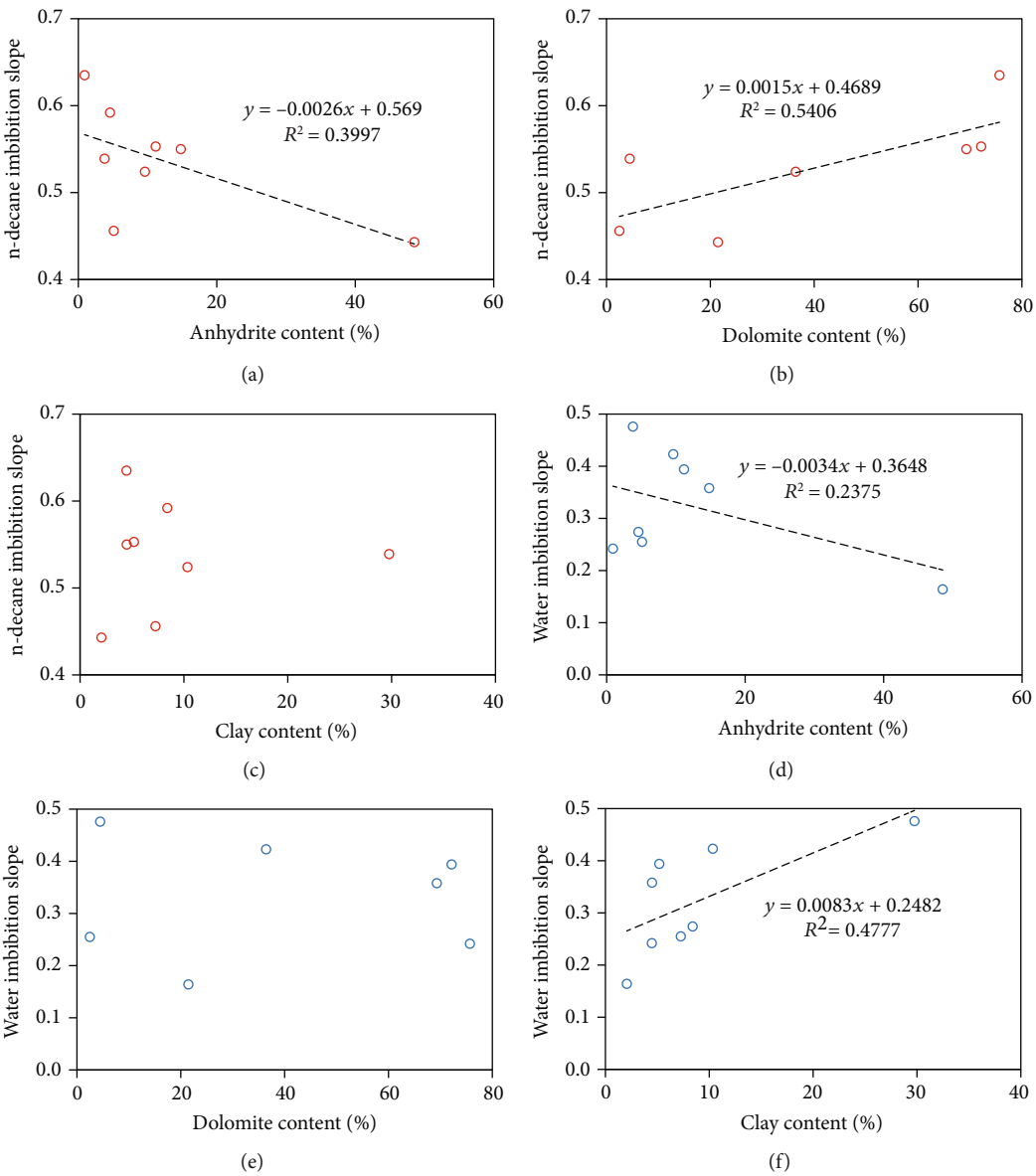

Figure 11: Crossplots of spontaneous imbibition parameters and mineral compositions of the Palaeogene Xiaganchaigou Formation samples from Qaidam Basin.

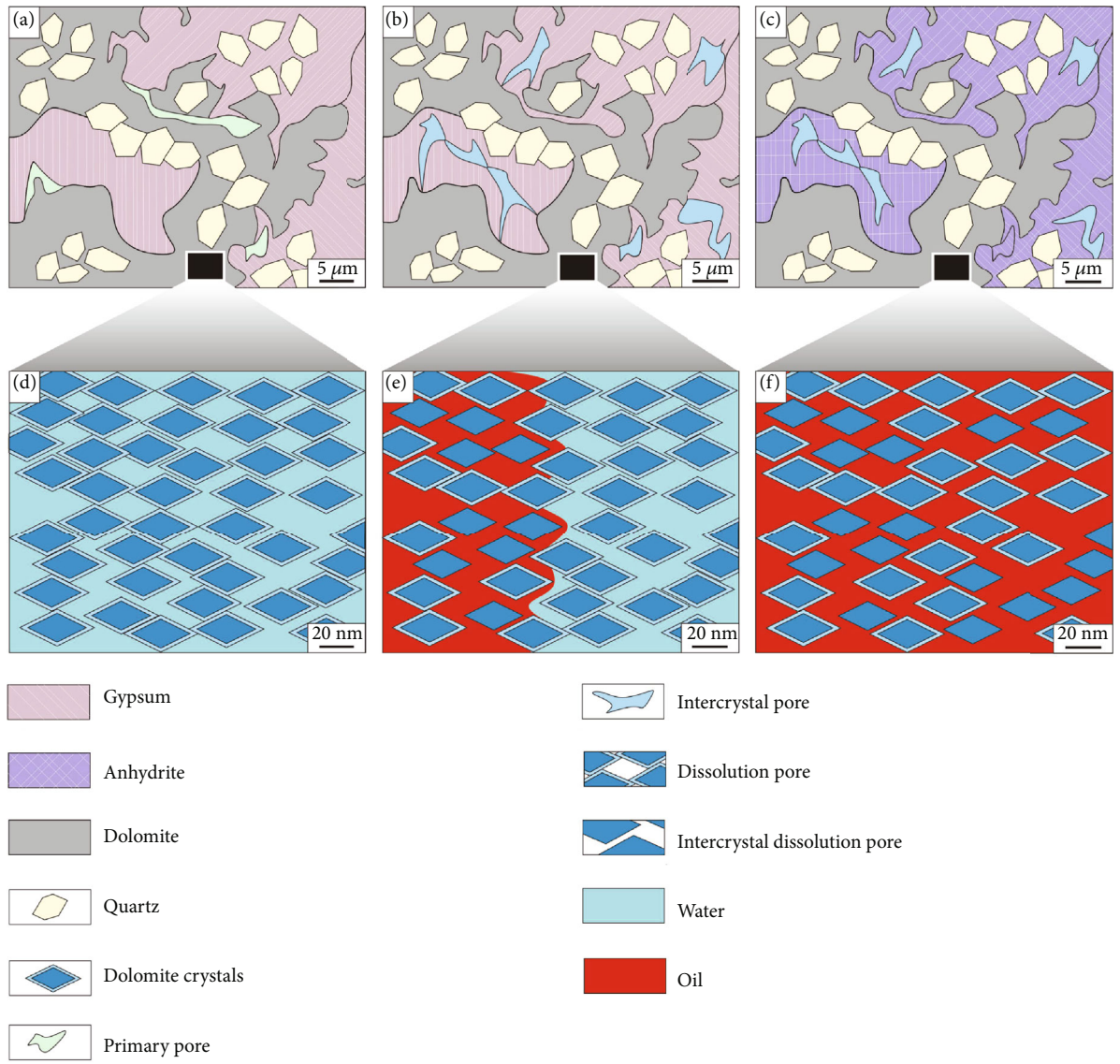

Figure 12: A genetic model for pore structure and connectivity of tight the mixed siliciclastic-carbonate sediment reservoirs.

properties of the samples from the upper member of the Xiaganchaigou Formation in the Yingxi Area and in combination with the depositional setting and diagenetic evolution sequence in this area.

At the early penecontemporaneous stage, the evaporation continuously strengthened as the palaeoclimate gradually became drier [47]. The lake basin water begins to recede and became more saline. The sulfate mineral components enter a saturated state [48]. Gypsum began to precipitate and fill between clastic grains and between clastic grains in carbonates, and the primary pores were filled (Figure 12(a)). The primary pores are destroyed. Meanwhile, the concentration of Mg^{2+} in water increased as the sulfate minerals precipitate [51–53]. The continuous infiltration of the high-salinity bittern experienced metasomatism of the carbonate sediments, which promoted dolomitization, and resulted in the large-scale development of the intercrystalline pores associated with the dolomitization (Figure 12(d)) [51–53]. The dolomite formed earlier has strong compaction pressure solubility resistance, inhibiting the damage to the reservoir caused by compaction and pressure dissolution. Intercrystalline pores are generally preserved in this way and provide space for the later migration and accumulation of fluid [53]. At the late penecontemporaneous stage, the level of the lake continued to fall as the water evaporation continued. The rapid and short-term fresh water dissolution occured in locally exposed topographic highlands [51]. Since the Yingxi Area was a $CaCO_3$-$CaSO_4$-H_2O-CO_2 diagenetic system, the atmospheric fresh water preferentially dissolved gypsum to form micrometer-sized dissolution pores (Figure 12(b)) [47, 48]. At the early diagenetic stage, with the increase in burial depth, the temperature and pressure of the formation also increased, and the gypsum was transformed into anhydrite by dehydration [47]. Since the cement of anhydrite is strong, the micrometer-sized dissolution pores in gypsum are sealed in anhydrite (Figure 12(c)). Consequently, micrometer-sized pores are controlled by the spatial distribution of anhydrite minerals. And the spatial

distribution is highly heterogeneous. There are well connected micropores in anhydrite, but their contribution to the overall connectivity of the reservoir is extremely limited. At the mid diagenetic stage (Figure 12(e)), the organic acid fluid from the source rocks is injected into the reservoir for the dissolution of the dolomite minerals already formed [51, 58]. On the basis of nanometer-sized intercrystalline pores, dolomite intercrystalline increased, and pores are formed to connect the relatively isolated intercrystalline dissolution pores (Figure 12(f)). A great number of the intercrystalline dissolution pores can be preserved for they are formed late and protected by hydrocarbon fluid [58]. Since the content of dolomites is high and they are equally distributed, the spatial distribution of nanoscale intercrystalline pores and intercrystalline dissolution pores in dolomite is also homogeneous.

Since the mineral composition of mixed siliciclastic-carbonate tight reservoirs is complex, the spatial distribution is highly heterogeneous. According to the classification of mixed siliciclastic-carbonate tight reservoirs in Section 4.1.2, different types of tight reservoirs provide different reservoir spaces and migration channels for oil and gas. The main reservoir space in LDR is dominated by intercrystalline pores and intercrystalline dissolution pores. The pores are numerous and are equally distributed. Meanwhile, intercrystalline dissolution pores also provide favorable tight oil migration channels for reservoirs. The main reservoir space in reservoirs of SCR and MSCR is dominated by the dissolution pores in anhydrite. The spatial distribution of pores is highly heterogeneous. The pore throat system in the anhydrite is developed, but its contribution to the overall connectivity of the reservoir is extremely limited. Dominant channel cannot be provided for the migration of tight oil. Moreover, the internal dissolution pores cannot act as the reservoir space for tight oil. Therefore, LDR is the high-quality tight oil reservoirs in the upper member of Xiaganchaigou Formation in Yingxi Area.

6. Conclusions

The micrometer-sized pores in mixed siliciclastic-carbonate tight reservoirs are dominated by the dissolution pores formed by the gypsum dissolution at the penecontemporaneous stage and are well preserved in anhydrite at the diagenetic stage. The average pore radius range, average throat radius range, and average coordination number range of micronmeter-sized pores are 2.09~3.42 μm, 1.32~2.19 μm, and 0.48~1.49, respectively. Restricted by the concentrated distribution of local clumps in the anhydrite, the spatial distribution of pore structure shows high heterogeneity. The pore connectivity is well developed in anhydrite. Nevertheless, under the strong cementation of anhydrite, the contribution of the throat system in the anhydrite to the reservoir is extremely limited.

The nanometer-sized pores in mixed siliciclastic-carbonate tight reservoirs mainly are the intercrystalline pores formed by the dolomitization at the penecontemporaneous stage. The range of nanometer-sized pores diameters is mainly distributed in 1.73-31.47 nm. The pore has a smooth surface, simple structure, and relatively homogeneous spatial distribution. At the diagenetic stage, a large number of intercrystalline dissolution pores were formed by the dissolution of carbonates by acidic fluids and connected the isolated intercrystalline pores of dolomite and increased the connectivity of oil-wetting pores in reservoirs.

Relatively developed nanometer-sized pores can be found in LDR. The spatial distribution of these nanometer-sized pores is highly homogeneous, and BJH TPV falls within the range of 0.003533~0.020521 $cm^3/(g{\cdot}nm)$, providing large reservoir space for the enrichment of tight oil. Meanwhile, the oil-wetting pores in LDR has well-developed connectivity and spontaneous imbibition slope of n-decane within the range of 0.55~0.635, providing advantageous migration channels for the filling of tight oil, making them high-quality tight oil reservoirs in the upper member of Xiaganchaigou Formation in the Yingxi Area.

Data Availability

The main data used to support the study is available within the article. If readers are interested in the data, you can communicate with corresponding author and obtain these data by email.

Conflicts of Interest

The authors declare that they have no conflicts of interest.

Authors' Contributions

Xin Wang and Tongzhi Lu contributed equally to this work.

Acknowledgments

This work is financially supported by the grants from the National Natural Science Foundation of China (No.41972147 and No. 42002050), the China Postdoctoral Science Foundation Funded Project (No. 2020M680815), the China University of Petroleum (Beijing) Research Startup Fund Project (No. ZX20200054), and the Supported by Science Foundation of China University of Petroleum, Beijing (No. 2462020XKBH009).

References

[1] Y. Dong, X. Zhu, S. Hua et al., "Genetic types and evolutionary model of mixed clastic-carbonate deposits in the lower part of the Sha-1 Formation, the Huanghua Depression," *Oil & Gas Geology*, vol. 32, pp. 98–107, 2011.

[2] R. Zhu, C. Zou, S. Wu et al., "Mechanism for generation and accumulation of continental tight oil in China," *Oil Gas Geology*, vol. 40, pp. 1168–1184, 2019.

[3] M. Myrow, "Mixed siliciclastic-carbonate deposition in an early cambrian oxygen-stratified basin, chapel island formation, southeastern newfoundland," *Journal of Sedimentary Research*, vol. 62, pp. 455–473, 1992.

[4] G. Brooks, L. Doyle, B. Suthard, S. Locker, and A. Hine, "Facies architecture of the mixed carbonate/siliciclastic inner continental shelf of west-Central Florida: implications for Holocene

barrier development," *Marine Geology*, vol. 200, no. 1-4, pp. 325–349, 2003.

[5] J. Mount, "Mixed siliciclastic and carbonate sediments: a proposed first-order textural and compositional classification," *Sedimentology*, vol. 32, no. 3, pp. 435–442, 1985.

[6] C. Brett and G. Baird, "Carbonate-shale cycles in the Middle Devonian of New York: An evaluation of models for the origin of limestones in terrigenous shelf sequences," *Geology*, vol. 13, no. 5, pp. 324–327, 1985.

[7] C. Yang and Q. Sha, "Sedimentary environment of the middle Devonian Qujing Formation, Qujing, Yunnan province: a kind of mixing sedimentation of terrigenous clastics and carbonate," *Acta Sedimentologica Sinica*, vol. 8, pp. 59–66, 1990.

[8] J. Martin-Chivelet, "Sequence stratigraphy of mixed carbonate-siliciclastic platforms developed in a tectonically active setting, Upper Cretaceous, Betic continental margin (Spain)," *Journal of Sedimentary Research*, vol. 65B, pp. 235–254, 1995.

[9] R. Dorsey and S. Kidwell, "Mixed carbonate-siliciclastic sedimentation on a tectonically active margin: example from the Pliocene of Baja California Sur, Mexico," *Geology*, vol. 27, no. 10, pp. 935–938, 1999.

[10] A. Campbell, "Shelf-geometry response to changes in relative sea level on a mixed carbonate- siliciclastic shelf in the Guyana Basin," *Sedimentary Geology*, vol. 175, no. 1-4, pp. 259–275, 2005.

[11] F. García-Hidalgo, J. Gil, and M. Segura, "Internal anatomy of a mixed siliciclastic–carbonate platform: the Late Cenomanian–Mid Turonian at the southern margin of the Spanish Central System," *Sedimentology*, vol. 54, no. 6, pp. 1245–1271, 2007.

[12] E. Gischler, R. Ginsburg, J. Herrle, and S. Prasad, "Mixed carbonates and siliciclastics in the quaternary of southern Belize: Pleistocene turning points in reef development controlled by sea-level change," *Sedimentology*, vol. 57, no. 4, pp. 1049–1068, 2010.

[13] T. Komatsu, H. Naruse, Y. Shigeta et al., "Lower Triassic mixed carbonate and siliciclastic setting with Smithian- Spathian anoxic to dysoxic facies, An Chau basin, northeastern Vietnam," *Sedimentary Geology*, vol. 300, pp. 28–48, 2014.

[14] S. Zhang, Y. Cao, R. Zhu et al., "Characterization of lacustrine mixed fine-grained sedimentary rocks using coupled chemostratigraphic-petrographic analysis: a case study from a tight oil reservoir in the Jimusar Sag, Junggar Basin," *Marine and Petroleum Geology*, vol. 99, pp. 453–472, 2019.

[15] T. Li, Z. Huang, Y. Feng et al., "Reservoir characteristics and evaluation of fluid mobility in organic-rich mixed siliciclastic-carbonate sediments: a case study of the lacustrine Qiketai Formation in Shengbei Sag, Turpan-Hami Basin, Northwest China," *Journal of Petroleum Science and Engineering*, vol. 185, p. 106667, 2020.

[16] J. Cai, E. Edmund, C. Cheng, and X. Hu, "Generalized Modeling of Spontaneous Imbibition Based on Hagen–Poiseuille Flow in Tortuous Capillaries with Variably Shaped Apertures," *Langmuir*, vol. 30, no. 18, pp. 5142–5151, 2014.

[17] J. Lai, G. Wang, Z. Wang et al., "A review on pore structure characterization in tight sandstones," *Earth-Science Reviews*, vol. 177, pp. 436–457, 2018.

[18] L. Anovitz and D. Cole, "Characterization and analysis of porosity and pore structures," *Reviews in Mineralogy & Geochemistry*, vol. 80, no. 1, pp. 61–164, 2015.

[19] Z. Diao, S. Li, W. Liu, H. Liu, and Q. Xia, "Numerical study of the effect of tortuosity and mixed wettability on spontaneous imbibition in heterogeneous porous media," *Capillarity*, vol. 4, no. 3, pp. 50–62, 2021.

[20] B. Bai, R. Zhu, S. Wu et al., "Multi-scale method of Nano(micro)-CT study on microscopic pore structure of tight sandstone of Yanchang Formation, Ordos Basin," *Petroleum Exploration Development*, vol. 40, no. 3, pp. 354–358, 2013.

[21] A. Ghanizadeh, C. Clarkson, S. Aquino, O. Ardakani, and H. Sanei, "Petrophysical and geomechanical characteristics of Canadian tight oil and liquid-rich gas reservoirs: I. Pore network and permeability characterization," *Fuel*, vol. 153, pp. 664–681, 2015.

[22] A. Giri, S. Tarafdar, P. Gouze, and T. Dutta, "Fractal pore structure of sedimentary rocks: simulation in 2-d using a relaxed bidisperse ballistic deposition model," *Journal of Applied Geophysics*, vol. 87, pp. 40–45, 2012.

[23] G. Desbois, J. Urai, P. Kukla, J. Konstanty, and C. Baerle, "High-resolution 3D fabric and porosity model in a tight gas sandstone reservoir:a new approach to investigate microstructures from mm- to nm-scale combining argon beam cross-sectioning and SEM imaging," *Journal of Petroleum Science and Engineering*, vol. 78, no. 2, pp. 243–257, 2011.

[24] L. Jiao, P. Ø. Andersen, J. Zhou, and J. Cai, "Applications of mercury intrusion capillary pressure for pore structures: a review," *Capillarity*, vol. 3, no. 4, pp. 62–74, 2020.

[25] J. Cai, Z. Zhang, W. Wei, D. Guo, S. Li, and P. Zhao, "The critical factors for permeability-formation factor relation in reservoir rocks: Pore-throat ratio, tortuosity and connectivity," *Energy*, vol. 188, article 116051, 2019.

[26] K. Higgs, H. Zwingmann, A. Reyes, and R. Funnell, "Diagenesis, porosity evolution, and petroleum emplacement in tight gas reservoirs, Taranaki Basin, New Zealand," *Journal of Sedimentary Research*, vol. 77, no. 12, pp. 1003–1025, 2007.

[27] K. Wu, C. Liao, X. Li et al., "Geological characteristics of hydrocarbon pool in Yingxiongling Structural Zone, Qaidam Basin," *Geoscience*, vol. 34, no. 2, pp. 378–389, 2020.

[28] J. Wang, Y. Wang, Z. Liu, J. Li, and P. Xi, "Cenozoic environmental evolution of the Qaidam Basin and its implications for the uplift of the Tibetan Plateau and the drying of Central Asia," *Palaeogeography, Palaeoclimatology, Palaeoecology*, vol. 152, no. 1-2, pp. 37–47, 1999.

[29] Z. An, J. Kutzbach, W. Prell, and S. Porter, "Evolution of Asian monsoons and phased uplift of the Himalaya-Tibetan plateau since Late Miocene times," *Nature*, vol. 411, no. 6833, pp. 62–66, 2001.

[30] A. Xiao, L. Wu, H. Li, and L. Wang, "Tectonic processes of the Cenozoic Altyn Tagh Fault and its coupling with the Qaidam Basin, NW China," *Acta Petrologica Sinica*, vol. 29, pp. 2826–2836, 2013.

[31] J. Pan, H. Li, Z. Sun, D. Liu, C. Wu, and C. Yu, "Tectonic responses in the Qaidam basin induced by Cenozoic activities of the Altyn Tagh fault," *Acta Petrologica Sinica*, vol. 31, pp. 3701–3712, 2015.

[32] C. Wu, C. Yan, H. Li et al., "Cenozoic tectonic evolution of the western Qaidam Basin and its constrain on the growth of the northern Tibetan Plateau," *Acta Petrologica Sinica*, vol. 29, pp. 2211–2222, 2013.

[33] F. A. Dullien, *Porous Media: Fluid Transport and Pore Structure*, Academic Press, Cambridge, MA, USA, 2012.

[34] M. He, Y. Zhou, K. Wu et al., "Pore network modeling of thin water film and its influence on relative permeability curves in tight formations," *Fuel*, vol. 289, p. 119828, 2021.

[35] Z. Wang, H. Li, X. Lan, K. Wang, Y. Yang, and V. Lisitsa, "Formation damage mechanism of a sandstone reservoir based on micro-computed tomography," *Advances in Geo-Energy Research*, vol. 5, no. 1, pp. 25–38, 2021.

[36] R. Ketcham, "Computational methods for quantitative analysis of three-dimensional features in geological specimens," *Geosphere*, vol. 1, no. 1, pp. 32–41, 2005.

[37] N. Alyafei, T. Mckay, and T. Solling, "Characterization of petrophysical properties using pore-network and lattice- Boltzmann modelling: choice of method and image sub-volume size," *Journal of Petroleum Science and Engineering*, vol. 145, pp. 256–265, 2016.

[38] A. Dabrowski, "Adsorption – from theory to practice," *Advances in Colloid and Interface Science*, vol. 93, no. 1-3, pp. 135–224, 2001.

[39] T. Li, Z. Huang, J. Zhao, X. Xu, and X. Guo, "Pore structure characteristics and their influencing factors: a case study from the middle jurassic mixed siliciclastic carbonate rocks, Turpan-Hami basin, Northwest China," *Journal of Petroleum Science and Engineering*, vol. 203, article 108611, 2021.

[40] E. Barrett, L. Joyner, and P. Halenda, "The determination of pore volume and area distributions in porous Substances. I. Computations from Nitrogen Isotherms," *Journal of the American Chemical Society*, vol. 73, no. 1, pp. 373–380, 1951.

[41] L. Chen, Z. Jiang, K. Liu, and F. Gao, "Quantitative characterization of micropore structure for organic-rich lower Silurian shale in the Upper Yangtze Platform, South China: implications for shale gas adsorption capacity," *Advances in Geo-Energy Research*, vol. 1, no. 2, pp. 112–123, 2017.

[42] Y. Li, Z. Wang, Z. Pan, X. Niu, Y. Yu, and S. Meng, "Pore structure and its fractal dimensions of transitional shale: a cross-section from east margin of the Ordos Basin, China," *Fuel*, vol. 241, pp. 417–431, 2019.

[43] Z. Gao and Q. Hu, "Initial water saturation and imbibition fluid affect spontaneous imbibition into Barnett shale samples," *Journal of Natural Gas Science and Engineering*, vol. 34, pp. 541–551, 2016.

[44] X. Zhang, "Classification and origin of mixosedimentite," *Geological Science and Technology Information*, vol. 19, pp. 31–34, 2000.

[45] L. Handy, "Determination of effective capillary pressures for porous media from imbibition data," *Aime*, vol. 219, no. 1, pp. 75–80, 1960.

[46] A. Hunt, R. Ewing, and B. Ghanbarian, "Percolation theory for flow in porous media," in *Lecture Notes in Physics 880*, p. 447, Springer, Heidelberg, Germany, 3rd edition, 2014.

[47] Y. Xiong, X. Tan, K. Wu, Q. Xu, Y. Liu, and Y. Qiao, "Petrogenesis of the Eocene lacustrine evaporites in the western Qaidam Basin: implications for regional tectonic and climate changes," *Sedimentary Geology*, vol. 416, p. 105867, 2021.

[48] R. Kuechler, K. Noack, and T. Zorn, "Investigation of gypsum dissolution under saturated and unsaturated water conditions," *Ecological Modelling*, vol. 176, no. 1-2, pp. 1–14, 2004.

[49] D. Loope, J. Mason, H. Bao, R. Kettler, and C. Zanner, "Deformation structures and an alteration zone linked to deposition of volcanogenic sulphate in an ancient playa (Oligocene of Nebraska, USA)," *Sedimentology*, vol. 52, no. 1, pp. 123–139, 2005.

[50] D. Ren, Z. Zhou, R. Liang, R. Zhou, N. Liu, and J. Nan, "Characteristics of clay minerals and its impacts on reservoir quality of tight sandstone gas reservoir: a case from Sulige Gas Field, Ordos Basin," *Lithologic Reservoirs*, vol. 31, no. 4, pp. 42–53, 2019.

[51] J. Feng, J. Cao, K. Hu et al., "Dissolution and its impacts on reservoir formation in moderately to deeply buried strata of mixed siliciclastic-carbonate sediments, northwestern Qaidam Basin, northwest China," *Marine & Petroleum Geology*, vol. 39, no. 1, pp. 124–137, 2013.

[52] C. Huang, J. Yuan, G. Tian, L. Wu, X. Pan, and Y. Hui, "The geochemical characteristics and formation mechanism of the Eocene lacustrine dolomite reservoirs in the western Qaidam," *Earth Science Frontiers*, vol. 23, no. 3, pp. 230–242, 2016.

[53] C. Huang, Z. Fan, J. Yuan, L. Wu, and G. Chen, "The characteristics of dolomite reservoir in saline lacustrine Basin, Qaidam, China," *Carbonates & Evaporites*, vol. 31, no. 3, pp. 307–317, 2016.

[54] L. Aylmore, M. Karim, and J. Quirk, "Dissolution of gypsum, monocalcium phosphate, and superphosphate fertilizers in relation to particle size and porous structure," *Australian Journal of Soil Research*, vol. 9, no. 1, pp. 21–32, 1971.

[55] K. Zhang, X. Pang, Z. Zhao et al., "Pore structure and fractal analysis of lower carboniferous carbonate reservoirs in the Marsel area, Chu-Sarysu basin," *Marine and Petroleum Geology*, vol. 93, pp. 451–467, 2018.

[56] X. Shao, X. Pang, H. Li, and X. Zhang, "Fractal analysis of pore network in tight gas sandstones using NMR method: a case study from the Ordos basin, China," *Energy & Fuels*, vol. 31, no. 10, pp. 10358–10368, 2017.

[57] R. Surdam, L. Crossey, E. Hagen, and H. Heasler, "Organic-inorganic interactions and sandstone diagenesis," *AAPG Bulletin*, vol. 73, no. 1, pp. 1–23, 1989.

[58] W. Zhang, X. Jian, L. Fu, F. Feng, and P. Guan, "Reservoir characterization and hydrocarbon accumulation in late Cenozoic lacustrine mixed carbonate-siliciclastic fine-grained deposits of the northwestern Qaidam basin, NW China," *Marine and Petroleum Geology*, vol. 98, pp. 675–686, 2018.

[59] X. Fan, G. Wang, Y. Li et al., "Pore structure evaluation of tight reservoirs in the mixed siliciclastic- carbonate sediments using fractal analysis of NMR experiments and logs," *Marine and Petroleum Geology*, vol. 109, pp. 484–493, 2019.